Moisture sources and dynamics over southeastern Tibetan Plateau reflected in dual water vapor isotopes

Zhongyin Cai[1*], Rong Li[1], Cheng Wang[1], Qiukai Mao[1], Lide Tian[1]

[1]Institute of International Rivers and Eco-security, Yunnan Key Laboratory of International Rivers and Transboundary Eco-security, Ministry of Education Key Laboratory for Ecosecurity of Southwest China, Yunnan University, Kunming, China

*Corresponding author: Zhongyin Cai (czypil@gmail.com and z.cai@ynu.edu.cn)

Abstract

The southeastern Tibetan Plateau (SETP) has experienced a significant drying trend in recent decades, likely linked to changes in moisture sources. Water vapor isotopes are valuable tracers of the atmospheric water cycle, yet their interpretation is hindered by ambiguities in atmospheric controls. To investigate the role of ocean surface evaporation, continental air mass intrusion, and rain-vapor interaction, we present a three-year daily time series of near-surface vapor $\delta^{18}O$ and *d*-excess from the SETP station. Our analysis reveals that apparent negative correlations between *d*-excess and relative humidity over the Indian Ocean are primarily driven by similar seasonal patterns, which become insignificant or marginal when examined seasonally. This result underscores the need for caution in interpreting *d*-excess as a conservative tracer of ocean surface evaporation. Instead, we identify local and upstream specific humidity as the primary determinant of non-monsoon season *d*-excess variability, influenced by the

intrusion of cold and dry air from upper levels. During the summer monsoon season, both *d*-excess and $\delta^{18}O$ reflect the effect of raindrop evaporation during transport, which decreases $\delta^{18}O$ but increases *d*-excess. These findings provide new insights into the use of water isotopes to track moisture sources and dynamics over the SETP, particularly under varying seasonal circulation systems. Particularly, the findings for *d*-excess will contribute to our understanding of different moisture sources and provide a framework for interpreting *d*-excess in various hydroclimatic applications, including ice core studies.

1 Introduction

The Tibetan Plateau (TP) and its surrounding regions, known as the Third Pole and the Asian Water Tower, plays a crucial role in supplying water to major Asian rivers, including the Mekong, Salween, Ganges, Yarlung Zangbo, among others, sustaining ecosystems and populations across the continent (Immerzeel et al., 2020; Yao et al., 2022). In recent decades, the water balance on the TP has undergone significant changes under the backdrop of global warming (Yao et al., 2022). Notably, the southeastern TP (SETP) is experiencing a drying trend while wetting in the north (Jiang et al., 2023; Zhang et al., 2023; Yao et al., 2022). Atmospheric water vapor is the primary input to the hydrological system, making it essential to understand its sources and dynamics to diagnose regional water imbalances. Using a Lagrangian vapor tracking method, Zhang et al. (2023) suggested that the drying trend is associated with meteorological droughts propagating from moisture source regions. However, their conclusions and methodology are subjects of ongoing debate (Zhang et al., 2025; Zhao et al., 2025). Water stable isotopes are natural tracers of the water cycle, offering valuable insights into moisture sources and dynamics (Bowen et al., 2019; Galewsky et al., 2016). These isotopes have been intensively studied on the TP in precipitation, surface water, and ice cores (Yao et al., 2013; Thompson et al., 2024; Bershaw, 2018). However, the interpretation of these isotopic

signals remains challenging due to complex fractionation processes and shifting circulation systems between summer monsoon and westerlies.

Recent studies have confirmed that monsoon convection at upstream along moisture transport pathways, rather than local precipitation amount, controls summer monsoon season precipitation $\delta^{18}O$ over southern TP (Cai et al., 2017; He et al., 2015). This is related to the "amount effect" (Dansgaard, 1964), where higher precipitation leads to lower $\delta^{18}O$ values due to continuous rainout associated with stronger convection, following the Rayleigh distillation (Cai and Tian, 2016; Scholl et al., 2009; Vuille et al., 2003). Additionally, interactions between rain and water vapor play a significant role in depleting the lower tropospheric vapor isotopes (Risi et al., 2008a; Kurita et al., 2011; Cai et al., 2018; Lee and Fung, 2008). While the regional amount effect prevails during the monsoon season, this relationship weakens or reverses in the non-monsoon season when it is dominated by westerlies. This variability suggests additional controls such as moisture source variability, kinetic fractionation, or shifts in atmospheric circulation patterns (Breitenbach et al., 2010; Cai and Tian, 2020; Guo et al., 2024; Yao et al., 2013).

Observations of vapor isotopes could help disentangle the different processes involved in the amount effect, particularly through examining the secondary parameter deuterium excess (*d*-excess). The *d*-excess, defined by Dansgaard (1964) as $\delta^{2}H - 8\delta^{18}O$, primarily reflects the effects of kinetic fractionation. During rainout process, equilibrium fractionation is the dominant mechanism, whereas raindrop evaporation is associated with kinetic fractionation. Further, limited precipitation during non-monsoon seasons makes it challenging to study a full seasonal cycle of the atmospheric water cycle, which can be compensated by continuous monitoring of vapor isotopes. While a few stations on the TP have monitored isotopic compositions in the vapor phase (Tian et al., 2020; Dai et al., 2021; Chen et al., 2024; Yu et al., 2016; Yu et al., 2015), there is limited knowledge about vapor *d*-excess.

Both theoretical predictions and observations over ocean surfaces indicate that *d*-excess reflects ocean surface evaporation conditions such as sea surface temperature (SST) and relative humidity normalized to SST (RH_{SST})

(Merlivat and Jouzel, 1979; Bonne et al., 2019; Liu et al., 2014; Craig and Gordon, 1965). These relationships are frequently invoked in interpreting *d*-excess over the TP (Zhao et al., 2012; Shao et al., 2021; Chen et al., 2024; Liu et al., 2024). For instance, Shao et al. (2021) showed significant correlations between an ice core *d*-excess record from the central TP and RH_{SST} over the northern Bay of Bengal (BOB) and Arabian Sea (AS). However, the correlation coefficient was only -0.44 with a steep slope of -0.99‰ $\%^{-1}$. This contrasts with oceanic regions where the slope typically ranges from -0.3‰ $\%^{-1}$ to -0.6‰ $\%^{-1}$ (Bonne et al., 2019; Liu et al., 2014; Benetti et al., 2014; Uemura et al., 2008), suggesting additional complexities over terrestrial areas. Moreover, many studies have suggested that *d*-excess at terrestrial sites is not a conservative tracer of evaporation conditions from oceanic source regions (Fiorella et al., 2018; Aemisegger et al., 2014; Welp et al., 2012; Wei and Lee, 2019; Samuels‐Crow et al., 2014). In addition, ice core *d*-excess values at high altitudes are generally higher than those observed in precipitation at lower altitudes on the TP (Shao et al., 2021; Tian et al., 2001; Zhao et al., 2012; Joswiak et al., 2013; Zhao et al., 2017; Thompson et al., 2000). The reason for this discrepancy remains unclear, highlighting the need for further research to understand the mechanism driving these differences.

Mountain valleys in the SETP are considered significant pathways for transporting water vapor into the TP (Araguás-Araguás et al., 1998; Tian et al., 2007; Yao et al., 2013). To investigate these processes, we initiated a water vapor sampling campaign at the South-East Tibetan Plateau Station for integrated observation and research of alpine environment (SETP station) in June 2015. We aim to study the moisture sources and dynamics and their influence on vapor isotope compositions across different seasons. To achieve these goals, we explored the relationships between vapor isotopes and oceanic evaporation conditions, continental air mass intrusions, as well as rain-vapor interactions during different seasons. Finally, we discuss the implications of our findings for interpreting ice core records.

2 Data and methods

2.1 Atmospheric water vapor sampling

Vapor samples were collected at the SETP station (29°46'N, 94°44'E, 3326 m above sea level, and Fig. S1) using a cryogenic trapping method. The sampling system includes an air pump, a linked-ball-shaped glass cold trap, and an electric-powered system that creates and maintains a cold environment filled by 95% ethanol as cold as below -80 °C. Ambient air was pumped from an inlet positioned about 8 m above ground level through a Teflon tube to a glass trap maintained at an operational temperature of -70 °C. The airflow rate was set to ~5 L/min, allowing the collection of 10-20 ml of water samples during each sampling session. Sampling durations were adjusted seasonally: 24 hours in summer and extended to 48 hours in winter when necessary to ensure adequate sample volume. Samples were collected at 20:00 Beijing Standard Time (12:00 UTC). The efficiency of the trapping method was verified by connecting an additional cold trap to the system, which showed no visible condensation in the additional cold trap (Yu et al., 2015). Further validation was achieved through comparisons with direct measurements using a Picarro L2130-i Cavity Ring Down Spectroscopy (CRDS) at Lhasa, southern TP, confirming the reliability of this method for atmospheric water vapor sampling (Tian et al., 2020).

The sampling campaign ran from 25 June 2015 to 14 June 2018, yielding a total of 742 samples. These samples were stored frozen until analysis. Samples collected before 28 June 2016 were measured at the Key Laboratory of Tibetan Plateau Earth System, Environment and Resources, Institute of Tibetan Plateau Research, Chinese Academy of Sciences by a Picarro L2130-i analyzer. Samples collected after 28 June 2016 were measured at the Institute of International River and Eco-security, Yunnan University by a Picarro L2140-i analyzer. The isotopic values were calibrated using three standard waters, with detailed calibration procedures described by Liu et al. (2024). The measurements are expressed relative to Vienna Standard Mean Ocean Water 2 (VSMOW2), with precisions of 0.1‰ for $\delta^{18}O$, 0.4‰ for $\delta^{2}H$, and 1.2‰ for *d*-excess.

2.2 Meteorological data

Daily local meteorological data prior to 2018, including precipitation amount, air temperature, air pressure, and relative humidity at the SETP station, were obtained from the National Tibetan Plateau/Third Pole Environment Data Center (Luo, 2018). Specific humidity (q) at the SETP station was calculated using air temperature, air pressure, and relative humidity data following established equations outlined in (Huang, 2018). Consistent with Yao et al. (2013), we defined June-September (JJAS) as the summer monsoon season. In contrast, November-April (Nov-Apr) was designated as the non-monsoon season, with May and October considered transition periods between the two seasons.

We further obtained meteorological variables such as 2-meter air temperature, 2-meter dew point temperature, SST, and others at 0.25°×0.25° and hourly resolution from the European Centre for Medium-Range Weather Forecasts fifth generation reanalysis (ERA5) (Hersbach et al., 2019). RH_{SST} is estimated using ERA5 data: $RH_{SST} = e_{air}/e_{sat}$, where e_{air} is vapor pressure of air and e_{sat} is saturation vapor pressure with respect to SST. Additionally, precipitation data at 0.1°×0.1° and half-hourly resolution were obtained from the Integrated Multi-satellitE Retrievals for GPM (V07) dataset (Huffman et al., 2023). Moreover, meteorological data at 1°×1° and 3-hourly resolution from the Global Data Assimilation System (GDAS) were used to calculate backward trajectories (see Section 2.4 for details).

Statistical analyses primarily involved linear correlations and regressions, with the coefficient of determination (R^2) used to quantify the variance explained by each variable. In addition, we also used composite analysis to reveal relationships between variables. For example, to identify general patterns in backward trajectories associated with d-excess exceeding 30‰, all the days with such high d-excess were compiled into a collection. A composite map of trajectories from this collection was then constructed to reveal typical pathways under these conditions.

2.3 Theoretical framework for the understanding of isotope compositions and humidity

Besides complex atmospheric circulation models, the evolution of vapor isotope compositions during different moistening and dehydration processes can be predicted through a compilation of atmospheric processes such as condensation, mixing, and raindrop evaporation (Noone, 2012; Worden et al., 2007; Galewsky et al., 2016). These process shape distinct pathways of isotopic evolution in relation to atmospheric humidity.

The Rayleigh distillation model describes the progressive condensation of water vapor (Dansgaard, 1964). The isotope composition of remaining vapor, denoted as δ, can be expressed as $\delta = (1 + \delta_0)(q/q_0)^{\alpha-1} - 1$, where q is the specific humidity, and α is the fractionation factor. A subscript of 0 refers to the initial condition of the air mass. Raindrop evaporation introduces further complexity. As raindrops form at higher altitudes where vapor is depleted in heavy isotopes, their partial evaporation affects the surrounding vapor, leading to isotope values lower than those predicted by Rayleigh models (Risi et al., 2008a; Worden et al., 2007). This effect gives rise to "super-Rayleigh" trajectories, characterized by an inflated effective fractionation factor (α_e), defined as $\alpha_e = (1 + \phi)\alpha$, where ϕ quantifies deviations from equilibrium. Notably, Worden et al. (2007) and Noone (2012) have given different equations for such deviations, and this study aligns with the formulations by Noone (2012).

Air mass mixing also influences humidity and isotopic compositions through mass balance principles. When a dry air mass mixes with a moist one, the specific humidity of the mixed air can be described as $q = f_{dry}q_{dry} + f_{moist}q_{moist}$, where f represents the fraction of each air mass, with $f_{dry} + f_{moist} = 1$. Isotopic compositions are similarly derived by solving mass balance equations for the light and heavy isotopes, resulting in a hyperbolic relationship between δ and q. In other words, $\delta \times q$ and q should have a linear relationship in the mixing process (Fiorella et al., 2018). The intercept of the regression between δ and $1/q$ or the slope between $\delta \times q$ and q provides an estimate of the moist end member's isotope composition (Keeling, 1958).

Assuming a surface temperature of 25 °C and relative humidity of 85%, we utilize the evaporation model by

Craig and Gordon (1965) to determine the isotopic composition of ocean evaporation. This results in $\delta^{18}O$ = -11.5‰, $\delta^{2}H$ = -81.4‰, and *d*-excess = 10.6‰. These values serve as the wet end member for modeling moistening process through mixing with ocean evaporation. For the dry end member, we consider a dehydrated air mass from the Rayleigh curve at q = 0.5 g/kg, $\delta^{18}O$ = -60.3‰, and $\delta^{2}H$ = -418.0‰ (Fig. S2). The dehydration process via condensation is initiated at a relative humidity of 80% on the mixing line. Similarly, "super-Rayleigh" distillation involving partial rain evaporation also begins from this starting point. We explore two "super-Rayleigh" scenarios: Rain_evap_A assumes 2% rain evaporation, while Rain_evap_B assumes 5%, based on equations from Noone (2012). Additionally, we consider the influence of evapotranspiration over south Asia and the TP on atmospheric humidity and vapor isotope compositions over SETP. Quantifying isotopic compositions of land surface evapotranspiration is challenging. Given precipitation $\delta^{18}O$ over south Asia generally ranges from -1.0‰ to -5.0‰ (Bowen and Wilkinson, 2002; Terzer-Wassmuth et al., 2021) and transpiration constitutes two-thirds or more of evapotranspiration (Cao et al., 2022; Han et al., 2022; Good et al., 2015), we assume a $\delta^{18}O$ value of -5.0‰ as an upper bound for land surface evapotranspiration. Similarly, we assume a *d*-excess of 15.0‰ for this wet end member.

2.4 Backward trajectory and moisture source diagnostic

To investigate air mass transport and diagnose moisture sources and pathways toward SETP, we calculated backward trajectories using the Hybrid Single-Particle Lagrangian Integrated Trajectory model (HYSPLIT) (Stein et al., 2015). Trajectory calculations were driven by meteorological data from the GDAS. Air parcels were released from 5 locations: the study site and points displaced 0.2° in each cardinal direction. These releases occurred at 7 different vertical levels: 10, 50, 100, 200, 300, 400, and 500 m above ground level. For each day during the sampling campaign, trajectories were initiated every 3 hours to calculate 10-day backward trajectories, resulting in 280 trajectories per day. Geographical and meteorological variables, including location, pressure, temperature, specific humidity, rainfall amount, boundary layer height, and terrain height along the trajectories, were stored at hourly

intervals.

To quantify moisture contributions along trajectories to SETP's humidity, we applied the Lagrangian moisture source diagnostic method developed by Sodemann et al. (2008). This method uses mass balance principles along trajectories, interpreting increases in specific humidity (forward in time) as moisture uptake and decreases as moisture loss due to precipitation. It also accounts for the reduced contribution of earlier moisture uptake due to precipitation en route. We previously adapted this method to identify moisture sources for precipitation in sub-regions of South Asia and East Asia (Cai et al., 2018; Cai and Tian, 2020).

The diagnostic results indicated that approximately 5% of the moisture arriving at SETP remained unattributed, confirming that 10-day trajectories are sufficient to diagnose most moisture sources. Unlike previous applications focused on identifying evaporative moisture sources from the Earth's surface, this study emphasizes the contribution of air parcels themselves to SETP's humidity. This variable is readily available from the diagnostic method, where changes in air parcel contributions within the boundary layer between time steps represent moisture uptake from the surface.

The moisture contribution of an air parcel to SETP's humidity is a measure of the importance of upstream air. We calculated weighted-mean values for key variables by using the moisture contribution of the air parcel along trajectories as the weight. We also applied K-means clustering to group trajectories, helping to identify major transport pathways. When calculating the mean trajectory for each cluster and meteorological variables along each mean trajectory, the moisture contribution of the air parcel is also considered as the weight to calculate weighted-means.

3 Results

3.1 General characteristics of vapor $\delta^{18}O$, *d*-excess, and local meteorological variables

In general, $\delta^{18}O$ values are at lower levels during the summer monsoon season and higher levels during the non-monsoon season (Fig. 1a). Mean $\delta^{18}O$ values are -18.4‰ for the non-monsoon season, -23.3‰ for the summer monsoon season, -16.9‰ for May, and -22.8‰ for October. $\delta^{18}O$ shows a dramatic decrease at the onset of the summer monsoon. Conversely, from the end of the summer monsoon season to spring and early summer, $\delta^{18}O$ shows a gradual increase trend. Although the amount effect significantly influences this region, the seasonal variation of $\delta^{18}O$ does not strictly align with local precipitation patterns. For instance, while local precipitation ceases clearly after the summer monsoon (Fig. 1e), $\delta^{18}O$ remains at relatively low levels. This behavior is consistent with precipitation $\delta^{18}O$ in SETP, northeast India, and Bangladesh (Yao et al., 2013; Cai and Tian, 2020; Yang et al., 2017).

In contrast to $\delta^{18}O$, *d*-excess displays different seasonal dynamics. The *d*-excess values are lower during the summer monsoon season and higher during non-monsoon periods (Fig. 1b). Mean *d*-excess values are 18.3‰ for the non-monsoon season, 11.9‰ for the summer monsoon season, 13.7‰ for May, and 14.9‰ for October. However, the timing of seasonal transitions in *d*-excess differs from that of $\delta^{18}O$. The highest *d*-excess values generally occur during winter months when air temperature and relative humidity (RH) are at their lowest levels (Fig. 1c and 1d). Furthermore, *d*-excess starts to decrease in spring, earlier than the sharp drop in $\delta^{18}O$ at the onset of the summer monsoon.

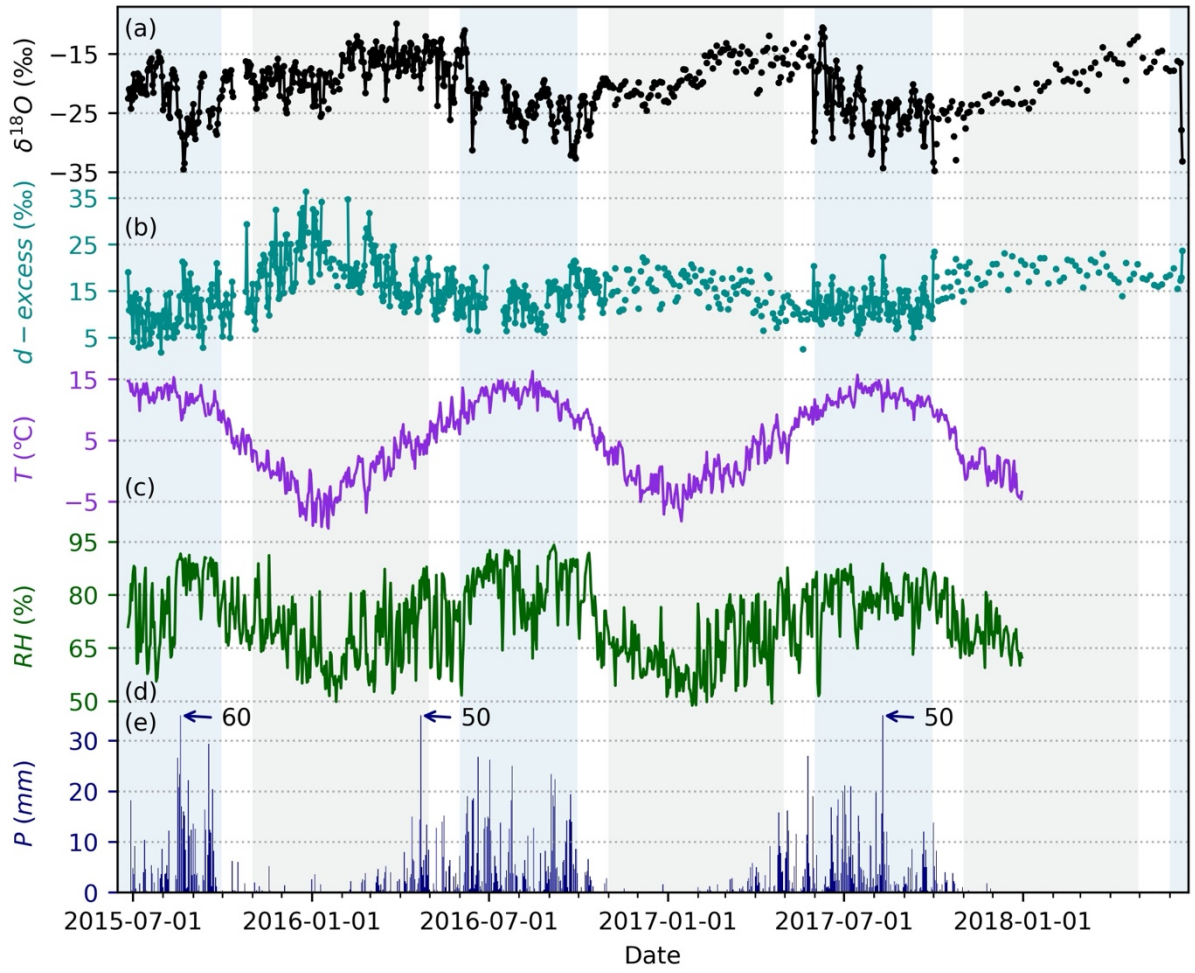

Figure 1. Time series of observed vapor $\delta^{18}O$, *d*-excess, and daily local meteorological variables from 2015-2018: (a) $\delta^{18}O$, (b) *d*-excess, (c) air temperature, (d) relative humidity (RH), and (e) precipitation amount. Light blue shading highlights the summer monsoon season, while light steel blue shading highlights the non-monsoon season.

The linear relationship between paired $\delta^{18}O$ and $\delta^{2}H$ values, along with their position relative to the global meteoric water line (GMWL, $\delta^{2}H = 8\delta^{18}O + 10$) (Craig, 1961), provides additional insights into isotopic fractionation processes (Putman et al., 2019). The local vapor line (LVL), estimated from all $\delta^{2}H$ and $\delta^{18}O$ data points, is $\delta^{2}H = 7.96\delta^{18}O + 14.04$ ($R^2 = 0.98$). This LVL plots above but approximately parallel with the GMWL. This relatively higher intercept of LVL reflects the continental location of the site and additional kinetic fractionation after ocean evaporation. The $\delta^{2}H$-$\delta^{18}O$ relationship also varied seasonally. During the non-monsoon season, the LVL

is $\delta^2H = 7.58\delta^{18}O + 10.61$ ($R^2 = 0.96$), while during the summer monsoon season, it shifts to $\delta^2H = 7.53\delta^{18}O + 0.91$ ($R^2 = 0.99$). Non-monsoon data primarily plot above both the GMWL and the overall LVL. Conversely, most monsoon season isotope data fall below the overall LVL, though the lowest δ-value points during this period are positioned above the overall LVL, suggesting additional kinetic fractionation such as rain evaporation (He et al., 2024). Vapor isotopes for May resemble those of the non-monsoon season but align more closely with both the GMWL and LVL, whereas data for October exhibit behaviors similar to the monsoon season observations.

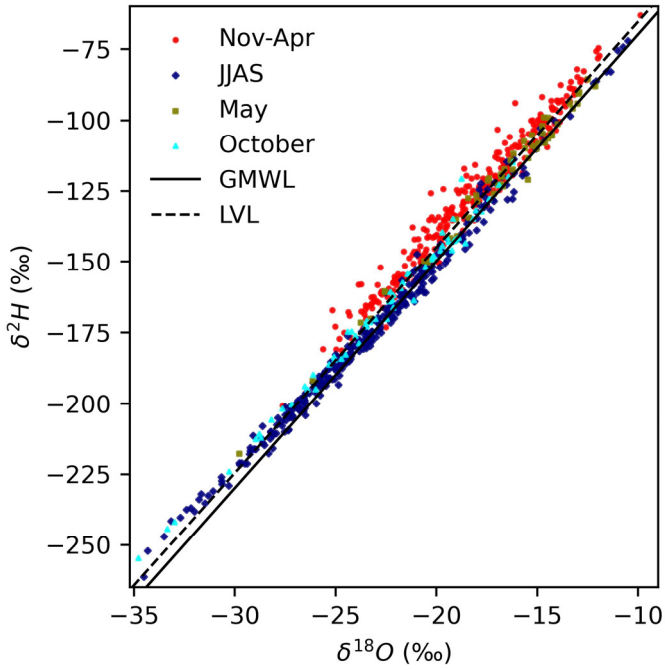

Figure 2. Relationship between vapor δ^2H and $\delta^{18}O$. The data is presented for different seasons: non-monsoon (Nov-Apr) as red dots, summer monsoon (JJAS) as navy diamonds, May as olive squares, and October cyan trangles. The solid line indicates the global meteoric water line (GMWL). The dashed line indicates the local vapor line (LVL) estimated from all δ^2H and $\delta^{18}O$ data points.

The relationships between $\delta^{18}O$ and specific humidity (q) further indicate distinct seasonal patterns in moisture dynamics (Fig. 3a). Due to unavilability of local meteorological data for 2018, our analyses focused on data collected before this year.. During the non-monsoon season, particularly in winter months, most data points are positioned above the Rayleigh distillation line but below a mixing line that represents an upper bound of

236 hypothetical evapotranspiration over South Asia. This suggests a mix between a dry end member and a moist end
237 member. In contrast, during the summer monsoon season, data predominately fall below the Rayleigh line,
238 influenced by "super-Rayleigh" processes linked to rain evaporation.

239 Futher insights come from examing $\delta \times q$ versus q relationships, which highlight seasonal contrasts in
240 moisture source signatures (Fig. S3). For the non-monsoon season, a simple estimation through the linear regression
241 between $\delta \times q$ and q suggests a moist end member with an $\delta^{18}O$ of -13.9‰ ± 0.6‰. The amount weighted annual
242 mean precipitation $\delta^{18}O$ at our site was about -14.5‰ (Yao et al., 2013). However, during the monsoon season, the
243 overall estimation of $\delta^{18}O$ for the moist end member through the linear regression between $\delta \times q$ and q is
244 significantly lower at -30.9‰ ± 1.8‰, pointing to an additional moisture source from rain evaporation that is more
245 depleted in heavy isotopes. These results align with the distribution of $\delta^{18}O$-q data below the Rayleigh line during
246 the summer monsoon season (Fig. 3a), underscoring the influence of different moisture sources and processes across
247 seasons.

248 The relationships between *d*-excess and q also reflect seasonal contrasts in moisture dynamics (Fig. 3b). During
249 non-monsoon season months, a negative correlation is observed where lower q corresponds to higher *d*-excess
250 values (Figs. 1 and 3b). This relationship is particularly pronounced under dry and cold conditions. In contrast,
251 during the summer monsoon season, no clear relationship between *d*-excess and q is apparent, with *d*-excess
252 showing considerable variability of approximately 20‰ at any given q. These findings suggest that *d*-excess is less
253 predictable using q compared to $\delta^{18}O$, except under low humidity levels.

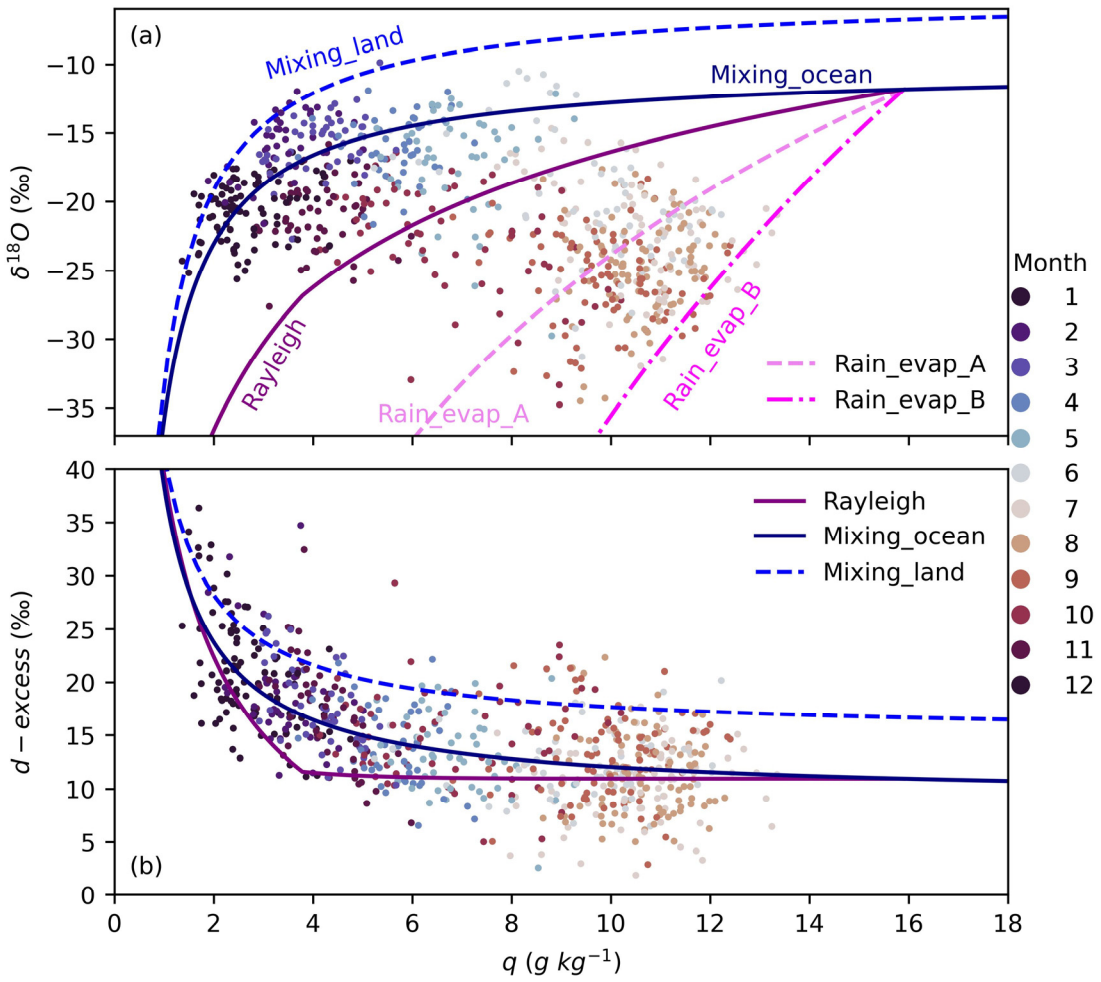

254

255 **Figure 3. Relationships between vapor isotopes ($\delta^{18}O$ and *d*-excess) and specific humidity (*q*) from 2015-**

256 **2017. (a) scatter plot of $\delta^{18}O$ against *q*. (b) scatter plot of *d*-excess against *q*. Each data point is color-coded**

257 **by month. Reference lines correspond to those in Fig. S2; their interpretations is detailed in Fig. S2 and**

258 **Section 2.3. Note that only data before 2018 are shown (see text for details).**

259 **3.2 Seasonal variability in moisture sources and transport pathways**

260 To understand the drivers behind the seasonal variations in moisture dynamics, we analyzed the moisture

261 sources and transport pathways during different seasons (Fig. 4). Our focus was on the contribution of moisture

262 from historical air masses (last 10 days) to humidity at SETP.

263 During the non-monsoon season, moisture is mainly transported via two pathways: one originating from the

264 west of SETP, carried by the westerlies (clusters Nov-Apr2 and Nov-Apr3), and another from the south, such as the

BOB (cluster Nov-Apr1). Quantitatively, the contributions frm these pathways are comparable, with 52.4% from the southern pathway and 47.7% from the western branches combined. Interestingly, when considering only trajectories without accounting for moisture contributions, all three clusters appear to originate from the west of SETP (Fig. S4). This discrepancy highlights the importance of distinguishing between pure air mass transport and actual moisture sources when interpreting trajectory data.

In contrast, during the summer monsoon season, moisture transport is predominantly from the south of SETP, driven by the summer monsoon. The pathways observed in May share similarities with those of the non-monsoon season, but with notable differences. Specifically, the second pathway during May (cluster May2) shifts southward toward the AS compared to its counterpart during the non-monsoon (cluster Nov-Apr2). Similarly, while October's air mass transport direction mirrors that of the non-monsoon, the moisture sources and pathways show greater alignment with those of the summer monsoon season, albeit with a slight eastward shift (Figs. 4d and S4d).

Another notable aspect of the moisture source distributions is the dominant contribution from proximal terrestrial regions, particularly those to the south of SETP (Fig. 4). For example, the 1% contour representing moisture contributions from air parcels over each 1°×1° grid box does not extend into oceanic regions during any of the four seasons. This indicates that surface evaporation from oceanic regions such as the BOB and AS contributes minimally. Instead, most of the moisture originating over these oceanic regions is lost through precipitation before reaching SETP, and what remains is replenished by evapotranspiration during transport over land. This finding raises an important question: do the vapor isotopes measured at SETP still reflect the meteorological conditions at their oceanic sources?

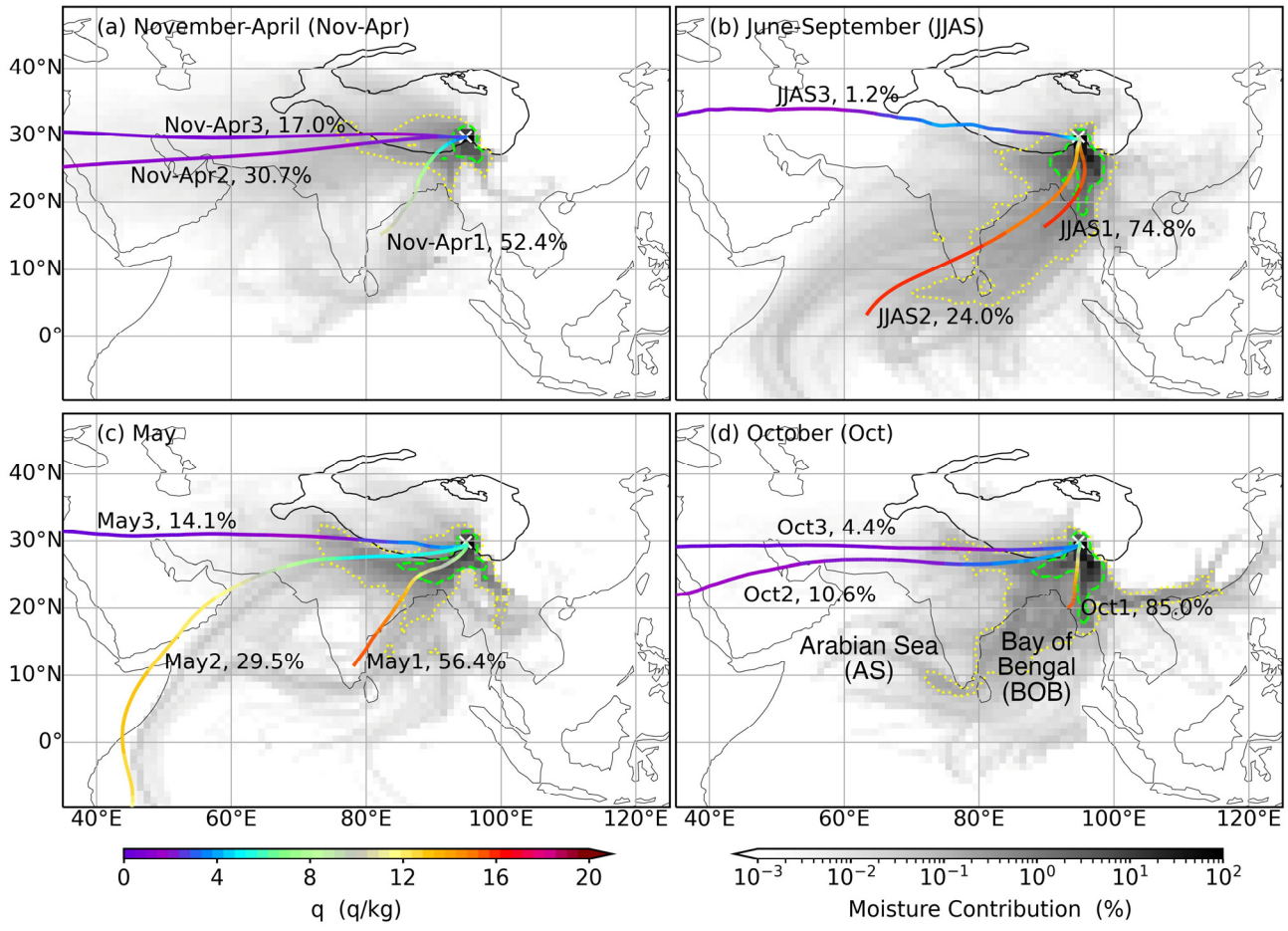

Figure 4. Moisture sources and transport pathways during different seasons from 2015-2017. (a) spatial distribution of relative contributions of moisture from all air parcels over each 1°×1° box (shading) to humidity at the SETP station, along with specific humidity (*q*) along mean trajectories (weighted by moisture contributions) for the non-monsoon season of November-April (Nov-Apr). (b-d) are the same as (a), but for the monsoon season of June-September (JJAS, b), May (c), and October (d), respectivley. The dotted yellow and dashed green contours indicate the moisture contribution at 0.1% and 1%, respectively. The yellow crosses indicate the location of the SETP station. The black solid lines denote the Tibetan Plateau with altitude contour at 3000 m.

3.3 Role of ocean surface evaporation conditions at seasonal and intraseasonal time scales

Relationships between *d*-excess and ocean surface evaporation conditions, such as RH_{SST} and SST, were

examined using data from 2015-2017 (Fig. 5a and Fig. S5a). Results indeed show negative correlations between *d*-excess and RH_{SST} over northern Indian Ocean, particularly in the northern parts of AS and BOB (Fig. 5a). Specifically, the regression slopes for this relationship across the northern Indian Ocean vary from higher than -0.1‰ $\%^{-1}$ to values below -0.6‰ $\%^{-1}$.

Focusing on specific regions, the northern BOB (10-22°N and 80-99°E) and the eastern AS (7-20°N and 65-78°E; Fig. 5a) exhibited regression slopes within the range (from -0.3‰ $\%^{-1}$ to -0.6‰ $\%^{-1}$) previously reported (Uemura et al., 2008; Benetti et al., 2014; Liu et al., 2014; Bonne et al., 2019). For instance, the regional average RH_{SST} in the eastern AS shows an overall regression slope of -0.49‰ $\%^{-1}$ ($r = -0.52$ and $p < 0.01$) (Fig. 6a), while the northern BOB has a slope of -0.52‰ $\%^{-1}$ ($r = -0.55$ and $p < 0.01$) (Fig. 6b). However, upon closer inspection of the *d*-excess- RH_{SST} plots (Fig. 6), it becomes evident that data points clustered according to different seasons, implying that the apparent negative correlations might primarily stem from opposing seasonal trends. Similarly, apparent negative correlations between *d*-excess and SST also emerge over the northern Indian Ocean (Fig. S5a). Yet, both theoretical prediction (Merlivat and Jouzel, 1979) and in-situ observations above the ocean surface (Bonne et al., 2019; Liu et al., 2014) suggest a positive correlation between *d*-excess and SST. These discrepancies lead us to speculate that the overall correlations between SETP vapor *d*-excess and surface evaporation conditions over the northern Indian Ocean are likely driven by seasonal variability.

The relationship between *d*-excess and RH_{SST} was further analyzed by distinguishing between the summer monsoon and non-monsoon seasons. During the summer monsoon season, the negative correlation diminishes significantly, with correlation coefficients dropping below 0.3 (Fig. 5b). In contrast, significant correlations present during the non-monsoon season (Fig. 5c), potentially due to intraseasonal variations where *d*-excess peaks in winter and decreases at the beginning and ending of the non-monsoon season (Fig. 1b), possibly accompanied by opposing RH_{SST} trends. However, even during the non-monsoon season, the explained variance in *d*-excess remains low, at a

maximum of 10%-16% over the northern BOB. Similarly, correlations with SST over the northern Indian Ocean also become negligible when seasons are considered separately (Fig. S5). In summary, vapor *d*-excess at SETP is less likely a conservative tracer of surface evaporation conditions (neither RH_{SST} nor SST) over the northern Indian Ocean. Therefore, interpreting *d*-excess in meteoric water or paleo archives from the TP as a proxy for Indian Ocean evaporation conditions should be approached with caution.

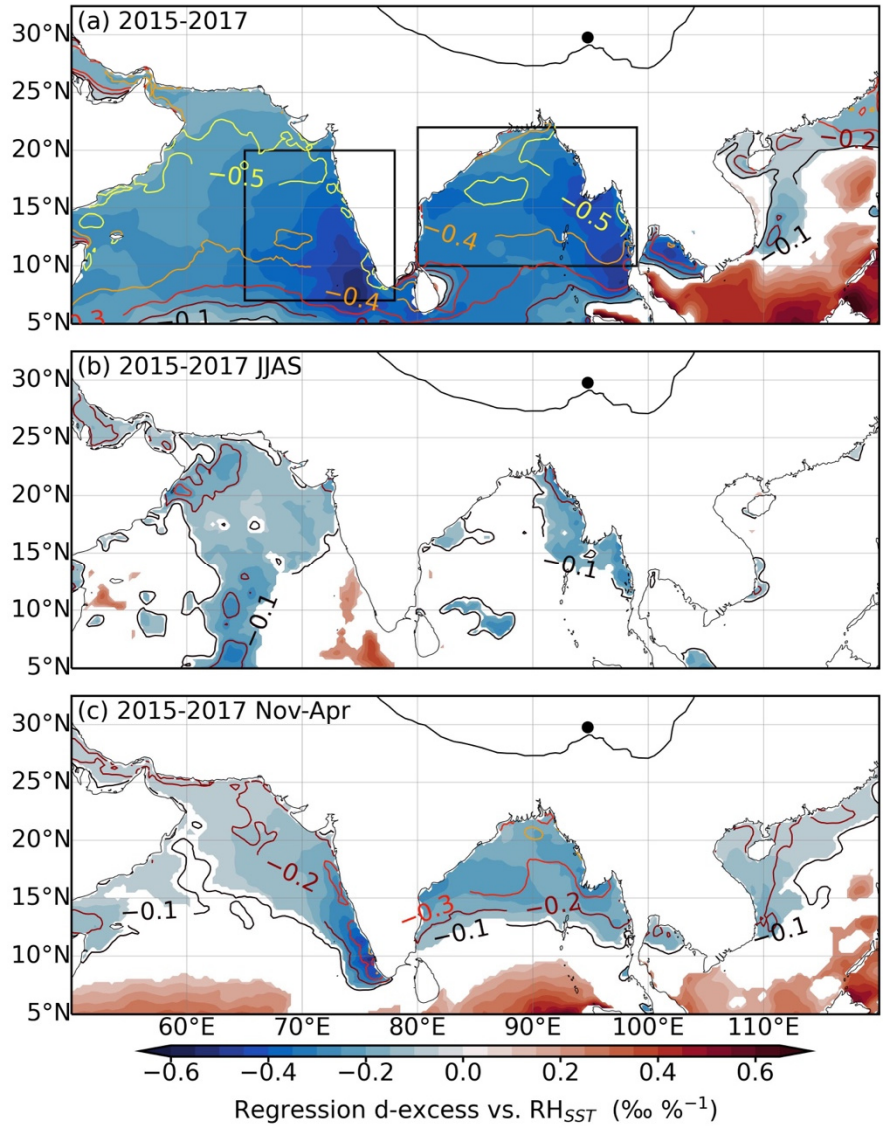

Figure 5. Relationships between vapor *d*-excess and relative humidity scaled to sea surface temperature (RH_{SST}). (a) regression of *d*-excess against RH_{SST} (shading and only values significant at the 95% significance level are shown) and correlation coefficients between them (contours at an interval of 0.1 and only negative

correlations are shown) for all the data from 2015-2017. (b) and (c) are the same as (a) but only for the data within the summer monsoon season (JJAS) or the non-monsoon season (Nov-Apr), respectively. The black dots indicate the location of the SETP station. The black solid lines denote the Tibetan Plateau with altitude contour at 3000 m.

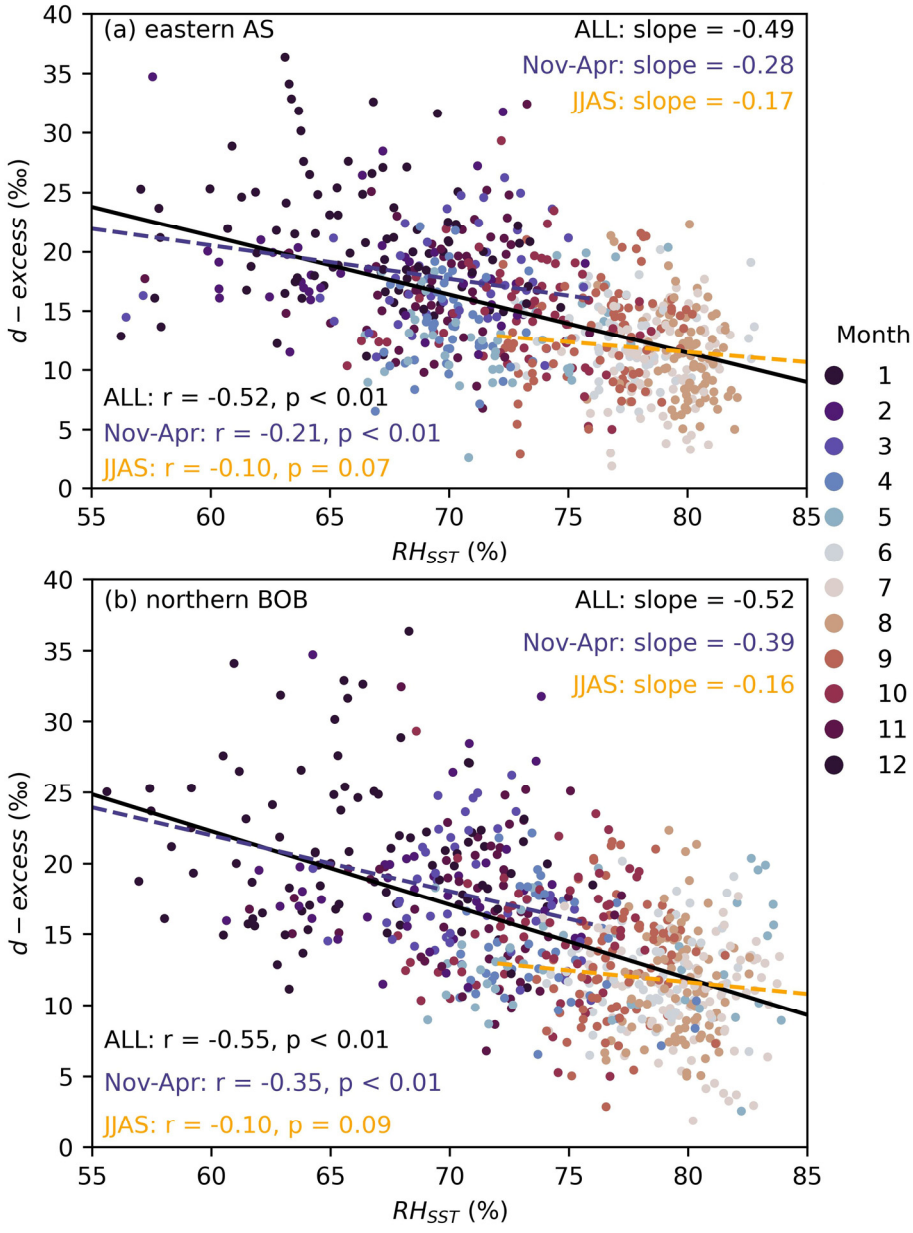

Figure 6. Relationships between SETP vapor *d*-excess and relative humidity normalized to sea surface temperature (RH_{SST}) averaged over (a) eastern Arabian Sea (7-20°N and 65-78°E) and (b) Bay of Bengal (10-22°N and 80-99°E) from 2015-2017. Each data point is color-coded by month. Solid black lines indicate the

linear regression between all data points. Dashed orange lines indicate linear regression for data during the non-monsoon season (Nov-Apr) and dashed dark blue lines for data during the summer monsoon (JJAS). The slope (‰ %$^{-1}$), r, and p values for the three data groups are also shown.

3.4 Role of dry and cold air intrusion during the non-monsoon season

Both theoretical predictions from the Rayleigh model and observations during the non-monsoon season suggest that *d*-excess increases as *q* decreases when *q* reaches extremely low values (Fig. 2). In addition, results for both air mass transport and moisture transport show the dominant role of the westerlies (Figs. S4a and 4a). Based on these evidences, we propose that during the non-monsoon season, vapor isotopes are influenced by the mixing of cold and dry air transported by westerlies from higher altitudes with surface vapor. Furthermore, surface vapor influenced by recycled moisture from terrestrial evapotranspiration would further elevate *d*-excess at a given *q* (Fig. 3b).

We performed a composite analysis on moisture sources and transport pathways for the highest (higher than 30‰, and n = 10) and lowest (lower than 10‰, and n = 8) *d*-excess observations during the non-monsoon season (Fig. 7). High *d*-excess values are primarily associated with moisture transported by westerlies from regions west of SETP, such as over the TP and northwestern India. In addition, backward trajectories for these cases show air masses characterized by extremely low *q*, reaching below 2 g kg^{-1} along the mean trajectories (weighted by moisture contribution) over the TP (Fig. 7a). Conversely, for low *d*-excess cases, a significant portion of moisture transport pathways shifts toward more humid regions, including northeast India, Bangladesh, and the BOB, with the L1 cluster accounting for 39.2% (Fig. 7b). This contrasting moisture transport pattern between high and low *d*-excess cases aligns with our hypothesis that high *d*-excess is associated with dry and cold air transported by westerlies.

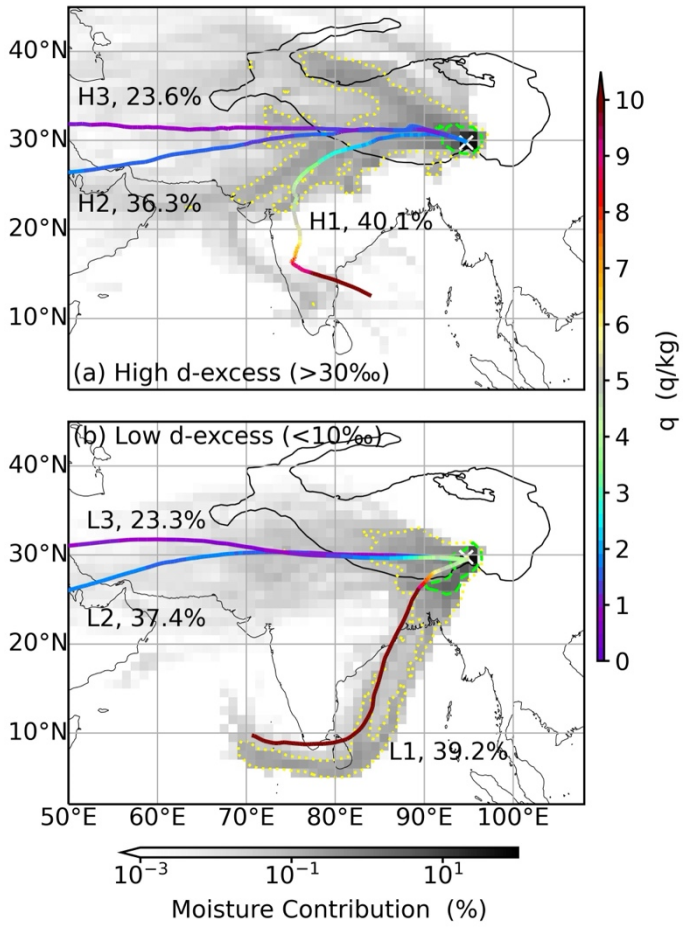

353

354 **Figure 7. Composite of moisture sources and transport pathways for high and low *d*-excess days during**
355 **the non-monsoon season of November-April. (a) spatial distribution of relative contribution of moisture from**
356 **all air parcels over each 1°×1° box (shading) to humidity at the SETP station, along with specific humidity (*q*)**
357 **along mean trajectories (weighted by moisture contributions) for *d*-excess values higher than 30‰ during the**
358 **non-monsoon season (n = 10). (b) is the same as (a) but for *d*-excess lower than 10‰ (n = 8). The yellow crosses**
359 **indicate the location of the SETP station. The black solid lines denote the Tibetan Plateau with altitude**
360 **contour at 3000 m.**

361 The influence of cold and dry air intrusions was further investigated through an analysis of relationships
362 involving *d*-excess, local *q*, weighted-mean upstream *q*, weighted-mean upstream air temperature, and weighted-
363 mean upstream air altitude (Fig. 8). Upstream variables represent weighted averages along the 10-day backward
364 trajectory, where weights correspond to the moisture contribution at each time step (Section 2.4). The non-monsoon

365 season *d*-excess shows robust negative correlations with both local *q* (r = -0.65, p < 0.01) and upstream *q* (r = -0.67,
366 p < 0.01). Furthermore, low *q* is associated with air masses characterized by low temperatures and high altitudes
367 (Figs. 8c and 8d), which could also impact $\delta^{18}O$. Indeed, $\delta^{18}O$ during high *d*-excess cases is lower than during low
368 *d*-excess cases (at a significance level of 95.3%). The overall correlation coefficient between $\delta^{18}O$ and *d*-excess
369 during the non-monsoon season is -0.29 (p < 0.01). Notably, correlations between $\delta^{18}O$ and *q* are weaker compared
370 to those observed for *d*-excess, with local *q* showing r = 0.42 (p < 0.01) and upstream *q* showing r = 0.38 (p < 0.01).
371 The relationship between non-monsoon season $\delta^{18}O$ and humidity is mainly expressed as the relationship between
372 $\delta \times q$ and q (r = 0.82 for local *q* and r = 0.90 for upstream *q*). Spatial correlations between vapor isotopes ($\delta^{18}O$
373 and *d*-excess) and 2-meter air temperature as well as humidity measured by 2-meter dew point temperature also
374 support these findings (Fig. S6). Significant negative correlations between *d*-excess and dew point temperature exist
375 over southeastern TP, northeast India, and northern Bangladesh. In contrast, $\delta^{18}O$ shows significant positive
376 correlations with air temperature over the India subcontinent and northwestern Southeast Asia.

377 As shown in Fig. 3b, extremely high *d*-excess values are predicted at very low *q* levels. Previous studies have
378 shown that as *q* approaches zero, vapor *d*-excess can approach 7000‰ following the Rayleigh distillation trajectory
379 (Bony et al., 2008), a behavior inherent to the definition of *d*-excess (Dütsch et al., 2017). High *d*-excess values
380 have also been observed in low humidity environments, such as polar regions (Bonne et al., 2014; Steen-Larsen et
381 al., 2017) and high altitudes (Samuels‐Crow et al., 2014; Webster and Heymsfield, 2003; Sayres et al., 2010;
382 Sodemann et al., 2017). Therefore, we infer that the increasing trend of *d*-excess with decreasing local *q*, upstream
383 *q,* and regional dew point temperature is due to enhanced mixing with dry and cold subsiding air transported by
384 westerlies from high altitudes. Relationships between upstream *q* and upstream air temperature as well as altitude
385 further support this inference, indicating that low humidity conditions are associated with the presence of subsiding
386 dry and cold air from high altitudes (Figs. 8c and 8d). Therefore, vapor *d*-excess during the non-monsoon not only

provides insights into specific humidity levels but also indicates the source of humidity.

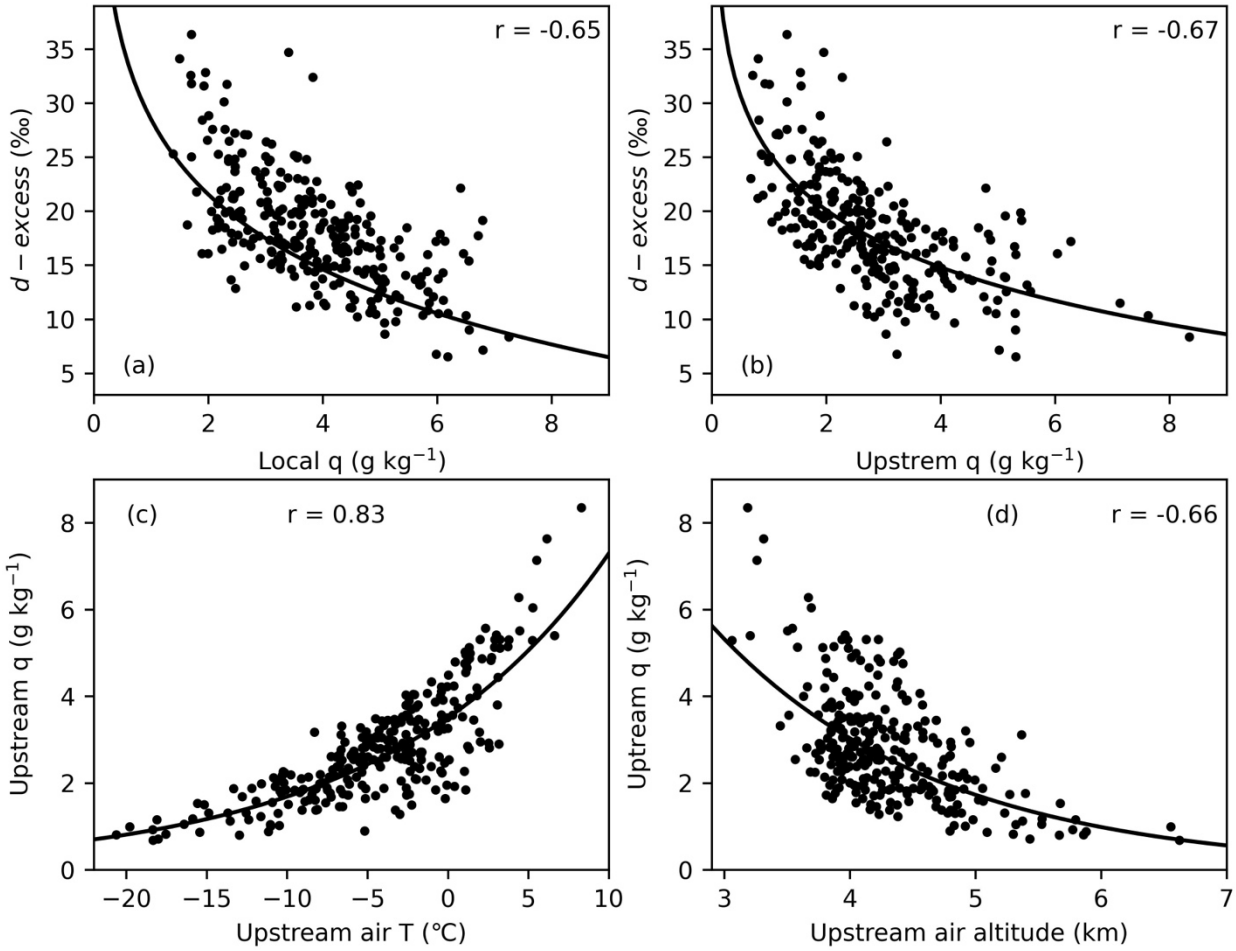

Figure 8. Relationships among vapor *d*-excess, local specific humidity (*q*), weighted-mean upstream *q*, weighted-mean upstream air temperature (T), and weighted-mean upstream air altitude during the non-monsoon season of November-April. (a) scatter plot of *d*-excess against local *q*. (b) scatter plot of *d*-excess against upstream weighted-mean *q*. (c) scatter plot of upstream *q* against upstream air T. (d) scatter plot of upstream *q* against upstream air altitude. All the upstream variables are mean values along backward trajectories weighted by the moisture contribution of air parcels. The solid curves indicate the log regression between the respective variables with the correlation coefficients indicated by the numbers.

3.5 Role of rain-vapor interaction during the summer monsoon season

In contrast to the significant dependence of *d*-excess on *q* during the non-monsoon season, vapor *d*-excess

shows no correlation with q (r = 0.04, p = 0.51) during the summer monsoon season. The behavior of $\delta^{18}O$ also differs between the two seasons (Fig. 3). During the summer monsoon season, $\delta^{18}O$-q plots below the Rayleigh curve, indicating that the vapor has undergone a degree of rain-vapor interaction due to evaporation (Fig. 3a). Partial rain evaporation in an unsaturated atmospheric environment leads to kinetic fractionation, which decreases *d*-excess values in raindrops while increasing *d*-excess in the surrounding vapor (Risi et al., 2008b). This effect of rain-vapor interaction on vapor isotopes has been suggested as a primary mechanism driving the amount effect in tropical regions (Risi et al., 2008a; Kurita et al., 2011; Bowen et al., 2019; Galewsky et al., 2016). Therefore, we hypothesize that vapor isotopes during the summer monsoon season at SETP are influenced by the degree of rain-vapor interaction.

The first evidence supporting this hypothesis is the significant correlation between $\delta^{18}O$ and *d*-excess during the summer monsoon season (r = -0.55, p < 0.01; Fig. 9a). In addition, there is a trend where $\delta^{18}O$ and *d*-excess exhibit weaker correlations when $\delta^{18}O$ levels are high, and stronger correlations when $\delta^{18}O$ levels are low (Figs. 9a and S7). To explore this further, we categorized days with daily precipitation of at least 2 mm as "rainy days" and those with less than 2 mm as "non-rainy days". This distinction is based on the premise that rain-vapor interaction cannot occur in the absence of rainfall. The analysis reveals that $\delta^{18}O$ during rainy days is significantly lower than that during non-rainy days, while *d*-excess show the opposite trend ($p < 0.01$ for both $\delta^{18}O$ and *d*-excess; Figs. 9b and 9c). Furthermore, the correlation between $\delta^{18}O$ and *d*-excess becomes stronger on rainy days (r = -0.69, $p <$ 0.01), though a weaker negative correlation persists even on non-rainy days (r = -0.40, $p < 0.01$). Even when applying a stricter threshold of 0 mm for non-rainy days, the negative correlation between $\delta^{18}O$ and *d*-excess remains significant (r = -0.37, p < 0.01). Moreover, correlations with local precipitation amount are weak for both $\delta^{18}O$ (r = -0.31, p < 0.01) and *d*-excess (r = 0.26, p < 0.01). These findings lead us to infer that vapor isotopes during the summer monsoon season at SETP are influenced not only by local rain-vapor interactions but also by the history of

rain-vapor interactions that occurred before the vapor reached the region.

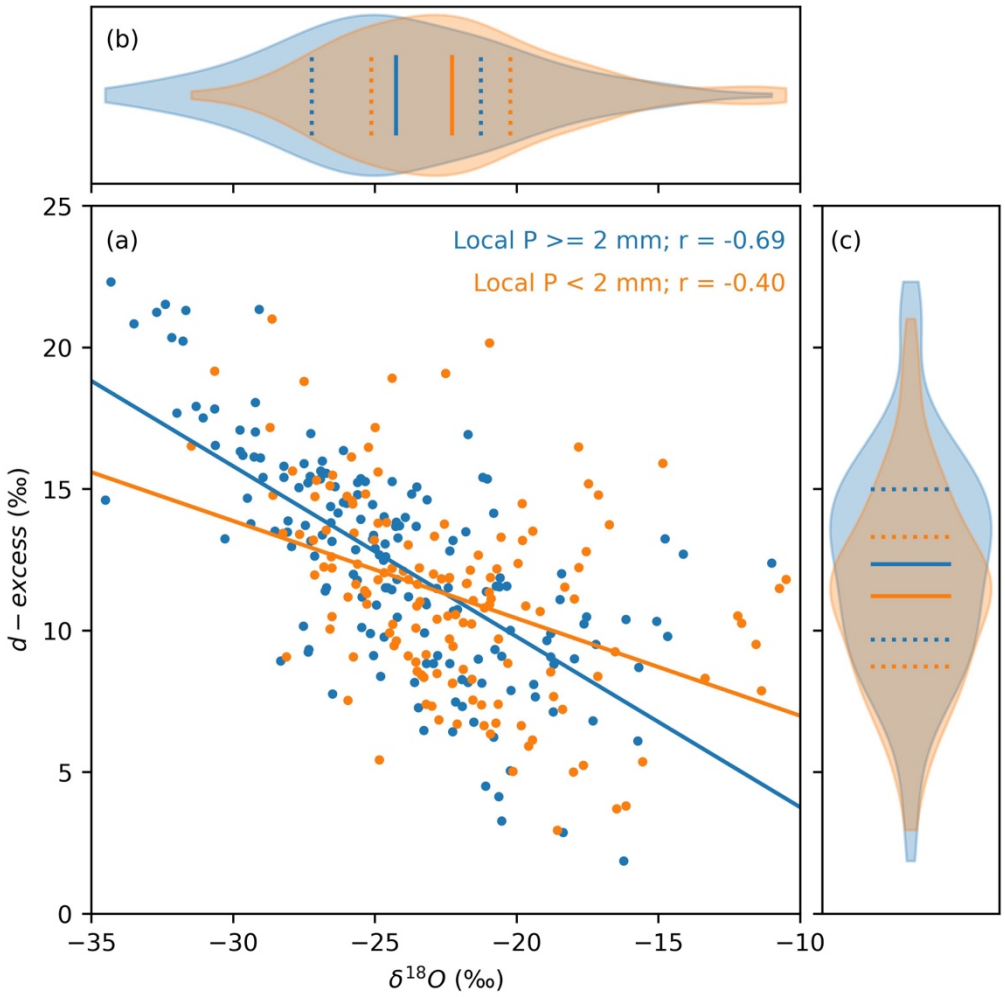

Figure 9. Relationships between SETP vapor *d*-excess and $\delta^{18}O$ during the summer monsoon season. (a) scatter plot of *d*-excess against $\delta^{18}O$ and linear regression lines between them. (b) distribution of $\delta^{18}O$ values with the dashed lines indicate values at the lower and upper quartiles and the solid lines indicate the mean values. (c) is the same as (b) but for *d*-excess. Orange colors indicate data observed during daily precipitation amount less than 2 mm and blue colors indicate data observed during days with precipitation amount not less than 2 mm. The r values for both lines are indicated in (a) and both of them are significant at the 0.01 level.

To further investigate the role of rain-vapor interactions, we use total precipitation amount (P_{acc}) as an indicator of rain-vapor interaction, considering the cumulative effect over several days preceding sampling. Our analysis

examined correlations between vapor isotopes ($\delta^{18}O$ and *d*-excess) and P_{acc} for periods ranging from 1-10 days prior to sampling (Figs. S8 and S9). Vapor *d*-excess reaches an optimal correlation with P_{acc} when considering 3 days before sampling (P_{acc_3d}). Vapor $\delta^{18}O$ shows a slightly longer memory and reaches an optimal correlation around 5-6 days before sampling. Fig. 10 shows the spatial distribution of these correlations, where *d*-excess positively correlates with P_{acc_3d} across a ~5°×5° region surrounding SETP and extending southwestward to the Himalayas (Fig. 10a). In contrast, $\delta^{18}O$ shows significant negative correlations in similar regions (Fig. 10b). Interestingly, even on non-rainy days, significant regional-scale correlations persist, albeit weaker and with a smaller spatial extent (Fig. S10).

These findings provide further evidence for understanding the mechanisms driving the amount effect. The negative correlation between $\delta^{18}O$ and P_{acc} has also been observed in precipitation and can be attributed to either continuous rainout (Scholl et al., 2009; Vuille et al., 2003; Ruan et al., 2019) or rain-vapor interactions (Lawrence et al., 2004; Risi et al., 2008a; Kurita et al., 2011; Worden et al., 2007). While continuous rainout, explained by the Rayleigh distillation model, accounts for the decreasing trend of $\delta^{18}O$ with increased rainfall, *d*-excess remains relatively stable unless specific humidity drops to very low levels (~4 g kg^{-1} in Fig. 3b for example). The positive correlation between vapor *d*-excess and P_{acc_3d} provides an additional constraint, suggesting that the amount effect is not solely a result of rainout but also involves rain-vapor interactions, which significantly influence vapor isotopes in the lower troposphere.

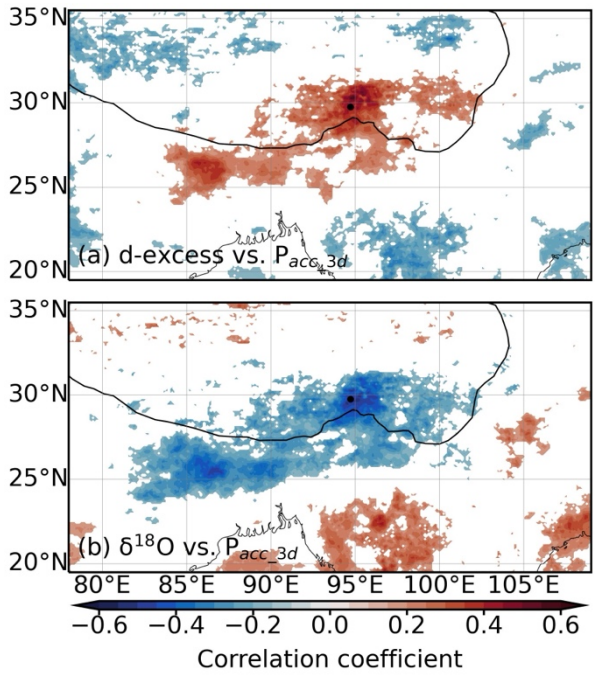

448

449 **Figure 10. Relationships between vapor isotops for rainy days (local daily precipitation amount not less**
450 **than 2 mm) and total precipitation amount at the regional scale during the summer monsoon season. (a)**
451 **spatial distribution of correlation coefficients between *d*-excess and total precipitation amount during 3 days**
452 **prior sampling (P_{acc_3d}). (b) is the same as (a) but for $\delta^{18}O$. Only values significant at the 95% significance**
453 **level are shown. The black dots indicate the location of the SETP station. The black solid lines denote the**
454 **Tibetan Plateau with altitude contour at 3000 m.**

455 **4 Implications for interpreting TP ice core isotope data**

456 Interpreting *d*-excess in meteoric water and ice cores on the TP is complicated by evaporation conditions over
457 the northern Indian Ocean (RH_{SST} and SST) and continental recycling (Shao et al., 2021; Zhao et al., 2012; Joswiak
458 et al., 2013; Pang et al., 2012; An et al., 2017). Attempts have been made to establish relationships between vapor
459 *d*-excess and RH_{STT} (Chen et al., 2024; Liu et al., 2024) as well as between ice core *d*-excess and RH_{STT} (Shao et al.,
460 2021) or SST (Zhao et al., 2012). Based on results in Section 3.3, however, the apparent relationships are primarily
461 a result of similarities in the seasonality of these variables.

462 Furthermore, the direct contribution of oceanic vapor to humidity at SETP is very limited (Fig. 4), implying an
463 even smaller contribution over the TP since SETP is at the forefront of moisture transport toward TP (Fig. S1). The
464 dominant terrestrial origin indicates significant continental recycling. Terrestrial processes such as transpiration and
465 evaporation introduce isotopically enriched moisture and high *d*-excess signatures, respectively. Mixing with
466 terrestrial sources is also reflected in the relationship between vapor isotopes and *q* (Fig. 3). Seasonal changes and
467 long-term variations in precipitation and ice core isotopes have been interpreted as shifts in moisture source between
468 recycled terrestrial moisture and oceanic sources or their relative contributions (An et al., 2017; Yang and Yao, 2020).
469 Oceanic moisture is typically associated with the summer monsoon, while westerlies bring moisture from
470 continental recycling or even the Mediterranean Sea. Water isotope signatures on the TP were thought to reflect this
471 interplay between the summer monsoon and westerlies (Joswiak et al., 2013; Pang et al., 2012; Tian et al., 2007).
472 Despite seasonally shifting moisture sources, continental recycling prevails throughout the year (Fig. 4). Our
473 alternative perspective explains high *d*-excess induced by westerlies as dry and cold air intrusions rather than surface
474 evaporation or evapotranspiration. While the interplay between the summer monsoon and westerlies remains valid,
475 but we emphasize changes in air mass properties driven by different circulation systems.

476 The proposed alternative interpretation could also help explain the abnormally high *d*-excess in high-altitude
477 ice cores mentioned in the Introduction. This is because specific humidity at these ice core sites is extremely low,
478 and prolonged interaction with cold and dry air may further modify snow isotope compositions (Ma et al., 2024;
479 Wahl et al., 2022). In addition, intense rain-vapor interactions during the summer monsoon represent another
480 potential source of elevated *d*-excess (Section 3.5). When this high *d*-excess vapor contributes to subsequent
481 precipitation, its signal can be inherited in the resulting precipitation (Risi et al., 2008b). However, a clear
482 relationship between TP precipitation *d*-excess and monsoon convection has yet to be established, partly due to
483 limited attention paid to *d*-excess in previous studies. On the other hand, local raindrop evaporation may counteract

this effect by reducing raindrop *d*-excess values. The overall positive correlation between precipitation *d*-excess and altitude across Asia has sometimes been attributed to stronger evaporation at lower altitudes (Bershaw, 2018). For snowfall on glaciers, however, evaporation for falling snowflakes is less likely due to cold temperatures and the short distance between the cloud base and the glacier surface. Therefore, elevated vapor *d*-excess signals caused by accumulated rain-vapor interactions at upstream associated with monsoon convection could be a possible source of the high *d*-excess in ice cores.

5 Conclusions

We present a three-year-long daily near-surface vapor isotope dataset observed at the SETP station, which is at the major channel for moisture entering the TP. The paired measurements of vapor isotopes and specific humidity reveal distinct moisture sources and dynamics between non-monsoon and summer monsoon seasons, consistent with findings from Lagrangian moisture diagnostic. Despite significant negative correlations between *d*-excess and relative humidity scaled to sea surface temperature over the northern Indian Ocean when all seasons are considered, these correlations weaken or even disappear when analyzed within individual seasons. This finding challenges the earlier interpretation of TP *d*-excess as indicator of oceanic evaporation conditions and guarantees new interpretations in the future.

During the non-monsoon season, vapor *d*-excess is primarily influenced by specific humidity at both local and upstream scales. Air that has undergone significant dehydration, situated at the lower end of the Rayleigh distillation, is expected to have extremely high *d*-excess values. Backward trajectory analyses and moisture source diagnostics reveal that the intrusion of cold and dry air driven by westerlies during the non-monsoon season leads to the increasing trend in *d*-excess as specific humidity decreases. This process also contributes to a weak negative correlation between *d*-excess and $\delta^{18}O$. Furthermore, $\delta^{18}O$ primarily reflects mixing processes involving a relatively

enriched moist end-member compared to the summer monsoon season. These new insights into vapor *d*-excess during the non-monsoon season provide an alternative framework for interpreting the high *d*-excess in high-altitude TP ice cores.

During the summer monsoon season, rain evaporation emerges as the dominant process shaping vapor isotope compositions. First, $\delta^{18}O$ systematically shifts below the Rayleigh distillation curve, aligning with predictions of "super-Rayleigh" distillation caused by partial rain evaporation. Second, $\delta^{18}O$ is anti-correlated with *d*-excess, pointing to kinetic fractionation as a source of depleted vapor, which cannot be attributed solely to rainout. Third, at the regional scale, $\delta^{18}O$ shows significant negative correlations with total precipitation amount, while *d*-excess positively correlates with total precipitation amount. These findings enhance our understanding of atmospheric humidity dynamics and help disentangle the different effects of rainout and rain-vapor interactions in the context of the amount effect.

This study reveals distinct moisture sources and dynamics between non-monsoon and monsoon seasons over the southeastern Tibetan Plateau. These findings will aid in interpreting $\delta^{18}O$ and *d*-excess records from Tibetan Plateau glaciers, offering refined insights into past hydroclimatic conditions and challenging assumptions linking ice core isotopes to oceanic evaporation alone.

Competing interests

The authors declare that they have no conflict of interest.

Acknowledgements

We thank the editors and the referees for their comments and suggesetions. This research was supported by the National Key R&D Program of China (Grant 2024YFF0807901), the National Natural Science Foundation of China (Grant 42371144), the Yunnan Fundamental Research Projects (Grant 202301AT070183), and the funding of

526 Donglu Talent Young Scholar from the Yunnan University and support for young scholars from the Double First-
527 Class Initiative for Ecological Disciplines of the Yunnan University. We would like to thank the staff at the South-
528 East Tibetan Plateau Station for integrated observation and research of alpine environment for their help in collecting
529 water samples and for sharing the meteorological data at the station.

530 **Data availability**

531 The NOAA ARL provided the HYSPLIT model and the GDAS data
532 (https://www.ready.noaa.gov/HYSPLIT.php). The Copernicus Climate Change Service provided the ERA5 data
533 (https://doi.org/10.24381/cds.adbb2d47 and https://doi.org/10.24381/cds.f17050d7). The GPM data are available
534 through GES DISC (https://doi.org/10.5067/GPM/IMERG/3B-HH/07). Local meteorological data at the SETP
535 station are provided by National Tibetan Plateau / Third Pole Environment Data Center
536 (https://dx.doi.org/10.11888/AtmosphericPhysics.tpe.68.db). The observation data at the SETP station have been
537 uploaded to Figshare and will be made publicly available after publication (10.6084/m9.figshare.27302871).

538 **Author contributions**

539 **Zhongyin Cai**: Conceptualization, methodology, investigation, formal analysis, funding acquisition, writing-
540 original draft, writing-review & editing; **Rong Li**: Investigation, data curation, writing-review & editing; **Cheng**
541 **Wang**: Validation; **Qiukai Mao**: Investigation, **Lide Tian**: Resources, project administration, funding acquisition.

542 **References**

543

544 Aemisegger, F., Pfahl, S., Sodemann, H., Lehner, I., Seneviratne, S. I., and Wernli, H.: Deuterium excess as a
545 proxy for continental moisture recycling and plant transpiration, Atmos. Chem. Phys., 14, 4029-4054, 10.5194/acp-
546 14-4029-2014, 2014.
547 An, W., Hou, S., Zhang, Q., Zhang, W., Wu, S., Xu, H., Pang, H., Wang, Y., and Liu, Y.: Enhanced Recent Local

548 Moisture Recycling on the Northwestern Tibetan Plateau Deduced From Ice Core Deuterium Excess Records, J.
549 Geophys. Res., 122, 12,541-512,556, 10.1002/2017jd027235, 2017.
550 Araguás-Araguás, L., Fröehlich, K., and Rozanski, K.: Stable isotope composition of precipitation over
551 southeast Asia, J. Geophys. Res., 103, 28721-28742, 1998.
552 Benetti, M., Reverdin, G., Pierre, C., Merlivat, L., Risi, C., Steen-Larsen, H. C., and Vimeux, F.: Deuterium excess
553 in marine water vapor: Dependency on relative humidity and surface wind speed during evaporation, J. Geophys.
554 Res., 119, 584-593, 2014.
555 Bershaw, J.: Controls on Deuterium Excess across Asia, Geosciences, 8, 257, 10.3390/geosciences8070257,
556 2018.
557 Bonne, J.-L., Behrens, M., Meyer, H., Kipfstuhl, S., Rabe, B., Schönicke, L., Steen-Larsen, H. C., and Werner, M.:
558 Resolving the controls of water vapour isotopes in the Atlantic sector, Nature Communications, 10, 1632,
559 10.1038/s41467-019-09242-6, 2019.
560 Bonne, J. L., Masson-Delmotte, V., Cattani, O., Delmotte, M., Risi, C., Sodemann, H., and Steen-Larsen, H. C.:
561 The isotopic composition of water vapour and precipitation in Ivittuut, southern Greenland, Atmos. Chem. Phys.,
562 14, 4419-4439, 10.5194/acp-14-4419-2014, 2014.
563 Bony, S., Risi, C., and Vimeux, F.: Influence of convective processes on the isotopic composition ($\delta^{18}O$ and δD)
564 of precipitation and water vapor in the tropics: 1. Radiative-convective equilibrium and Tropical Ocean–Global
565 Atmosphere–Coupled Ocean-Atmosphere Response Experiment (TOGA-COARE) simulations, J. Geophys. Res.,
566 113, D19305, 10.1029/2008JD009942, 2008.
567 Bowen, G. J. and Wilkinson, B.: Spatial distribution of $\delta^{18}O$ in meteoric precipitation, Geology, 30, 315,
568 10.1130/0091-7613(2002)030<0315:sdooim>2.0.co;2, 2002.
569 Bowen, G. J., Cai, Z., Fiorella, R. P., and Putman, A.: Isotopes in the Water Cycle: Regional- to Global-Scale
570 Patterns and Applications, Annu. Rev. Earth Planet. Sci., 47, 453-479, 10.1146/annurev-earth-053018-060220,
571 2019.
572 Breitenbach, S. F. M., Adkins, J. F., Meyer, H., Marwan, N., Kumar, K. K., and Haug, G. H.: Strong influence of
573 water vapor source dynamics on stable isotopes in precipitation observed in Southern Meghalaya, NE India, Earth
574 Planet. Sci. Lett., 292, 212-220, 10.1016/j.epsl.2010.01.038, 2010.
575 Cai, Z. and Tian, L.: Atmospheric controls on seasonal and interannual variations in the precipitation isotope
576 in the East Asian Monsoon region, J. Climate, 29, 1339-1352, 10.1175/JCLI-D-15-0363.1, 2016.
577 Cai, Z. and Tian, L.: What causes the post-monsoon ^{18}O depletion over Bay of Bengal head and beyond?,
578 Geophys. Res. Lett., 47, e2020GL086985, 10.1029/2020gl086985, 2020.
579 Cai, Z., Tian, L., and Bowen, G. J.: ENSO variability reflected in precipitation oxygen isotopes across the Asian
580 Summer Monsoon region, Earth Planet. Sci. Lett., 475, 25-33, 10.1016/j.epsl.2017.06.035, 2017.
581 Cai, Z., Tian, L., and Bowen, G. J.: Spatial-seasonal patterns reveal large-scale atmospheric controls on Asian
582 Monsoon precipitation water isotope ratios, Earth Planet. Sci. Lett., 503, 158-169, 10.1016/j.epsl.2018.09.028, 2018.
583 Cao, R., Huang, H., Wu, G., Han, D., Jiang, Z., Di, K., and Hu, Z.: Spatiotemporal variations in the ratio of
584 transpiration to evapotranspiration and its controlling factors across terrestrial biomes, Agr. Forest Meteorol., 321,
585 108984, 10.1016/j.agrformet.2022.108984, 2022.
586 Chen, M., Gao, J., Luo, L., Zhao, A., Niu, X., Yu, W., Liu, Y., and Chen, G.: Temporal variations of stable isotopic
587 compositions in atmospheric water vapor on the Southeastern Tibetan Plateau and their controlling factors, Atmos.
588 Res., 303, 10.1016/j.atmosres.2024.107328, 2024.
589 Craig, H.: Isotopic Variations in Meteoric Waters, Science, 133, 1702-1703, 10.1126/science.133.3465.1702,
590 1961.
591 Craig, H. and Gordon, L. I.: Deuterium and oxygen 18 variations in the ocean and the marine atmosphere, in:

Stable Isotopes in Oceanographic Studies and Paleotemperatures. Spoleto, Tongiorgi, E., Italy, 9-130, 1965.

Dai, D., Gao, J., Steen-Larsen, H. C., Yao, T., Ma, Y., Zhu, M., and Li, S.: Continuous monitoring of the isotopic composition of surface water vapor at Lhasa, southern Tibetan Plateau, Atmos. Res., 264, 10.1016/j.atmosres.2021.105827, 2021.

Dansgaard, W.: Stable isotopes in precipitation, Tellus, 16, 436-468, 10.1111/j.2153-3490.1964.tb00181.x, 1964.

Dütsch, M., Pfahl, S., and Sodemann, H.: The impact of nonequilibrium and equilibrium fractionation on two different deuterium excess definitions, J. Geophys. Res., 122, 12732-12746, 10.1002/2017JD027085, 2017.

Fiorella, R. P., Poulsen, C. J., and Matheny, A. M.: Seasonal Patterns of Water Cycling in a Deep, Continental Mountain Valley Inferred from Stable Water Vapor Isotopes, J. Geophys. Res., 123, 7271-7291, doi:10.1029/2017JD028093, 2018.

Galewsky, J., Steen-Larsen, H. C., Field, R. D., Worden, J., Risi, C., and Schneider, M.: Stable isotopes in atmospheric water vapor and applications to the hydrologic cycle, Rev. Geophys., 54, 809-865, 10.1002/2015RG000512, 2016.

Good, S. P., Noone, D., and Bowen, G.: Hydrologic connectivity constrains partitioning of global terrestrial water fluxes, Science, 349, 175-177, 10.1126/science.aaa5931, 2015.

Guo, H., Pang, H., Wu, S., Xu, T., Mutz, S. G., Zhan, Z., Lin, W., Zhang, W., and Hou, S.: Global abnormal precipitation 18O depletion during late/post monsoon season, Earth Planet. Sci. Lett., 641, 10.1016/j.epsl.2024.118815, 2024.

Han, J., Tian, L., Cai, Z., Ren, W., Liu, W., Li, J., and Tai, J.: Season-specific evapotranspiration partitioning using dual water isotopes in a Pinus yunnanensis ecosystem, southwest China, J. Hydrol., 608, 127672, 10.1016/j.jhydrol.2022.127672, 2022.

He, S., Jackisch, D., Feng, L., Samanta, D., Wang, X., and Goodkin, N. F.: Uncovering Below Cloud Rain-Vapor Interactions During Tropical Rain Events Through Simultaneous and Continuous Real-Time Monitoring of Rain and Vapor Isotopes, J. Geophys. Res., 129, e2023JD040084, https://doi.org/10.1029/2023JD040084, 2024.

He, Y., Risi, C., Gao, J., Masson-Delmotte, V., Yao, T., Lai, C.-T., Ding, Y., Worden, J., Frankenberg, C., Chepfer, H., and Cesana, G.: Impact of atmospheric convection on south Tibet summer precipitation isotopologue composition using a combination of in situ measurements, satellite data and atmospheric general circulation modeling, J. Geophys. Res., 120, 3852-3871, 10.1002/2014JD022180, 2015.

Hersbach, H., Bell, B., Berrisford, P., Horányi, A., J., M.-S., Nicolas, J., Radu, R., Schepers, D., Simmons, A., Soci, C., and Dee, D.: Global reanalysis: goodbye ERA-Interim, hello ERA5, 10.21957/vf291hehd7, 2019.

Huang, J.: A Simple Accurate Formula for Calculating Saturation Vapor Pressure of Water and Ice, Journal of Applied Meteorology and Climatology, 57, 1265-1272, https://doi.org/10.1175/JAMC-D-17-0334.1, 2018.

Huffman, G. J., Stocker, E. F., Bolvin, D. T., Nelkin, E. J., and Tan, J.: GPM IMERG Final Precipitation L3 Half Hourly 0.1 degree x 0.1 degree V07, Greenbelt, MD, Goddard Earth Sciences Data and Information Services Center (GES DISC) [dataset], 10.5067/GPM/IMERG/3B-HH/07, 2023.

Immerzeel, W. W., Lutz, A. F., Andrade, M., Bahl, A., Biemans, H., Bolch, T., Hyde, S., Brumby, S., Davies, B. J., Elmore, A. C., Emmer, A., Feng, M., Fernández, A., Haritashya, U., Kargel, J. S., Koppes, M., Kraaijenbrink, P. D. A., Kulkarni, A. V., Mayewski, P. A., Nepal, S., Pacheco, P., Painter, T. H., Pellicciotti, F., Rajaram, H., Rupper, S., Sinisalo, A., Shrestha, A. B., Viviroli, D., Wada, Y., Xiao, C., Yao, T., and Baillie, J. E. M.: Importance and vulnerability of the world's water towers, Nature, 577, 364-369, 10.1038/s41586-019-1822-y, 2020.

Jiang, J., Zhou, T., Qian, Y., Li, C., Song, F., Li, H., Chen, X., Zhang, W., and Chen, Z.: Precipitation regime changes in High Mountain Asia driven by cleaner air, Nature, 10.1038/s41586-023-06619-y, 2023.

Joswiak, D. R., Yao, T., Wu, G., Tian, L., and Xu, B.: Ice-core evidence of westerly and monsoon moisture

636 contributions in the central Tibetan Plateau, J. Glaciol., 59, 56-66, 10.3189/2013JoG12J035, 2013.
637 Keeling, C. D.: The concentration and isotopic abundances of atmospheric carbon dioxide in rural areas,
638 Geochim. Cosmochim. Acta, 13, 322-334, 10.1016/0016-7037(58)90033-4, 1958.
639 Kurita, N., Noone, D., Risi, C., Schmidt, G. A., Yamada, H., and Yoneyama, K.: Intraseasonal isotopic variation
640 associated with the Madden-Julian Oscillation, J. Geophys. Res., 116, D24101, 10.1029/2010JD015209, 2011.
641 Lawrence, J. R., Gedzelman, S. D., Dexheimer, D., Cho, H.-K., Carrie, G. D., Gasparini, R., Anderson, C. R.,
642 Bowman, K. P., and Biggerstaff, M. I.: Stable isotopic composition of water vapor in the tropics, J. Geophys. Res.,
643 109, D06115, 10.1029/2003JD004046, 2004.
644 Lee, J.-E. and Fung, I.: "Amount effect" of water isotopes and quantitative analysis of post-condensation
645 processes, Hydrol. Processes, 22, 1-8, 10.1002/hyp.6637, 2008.
646 Liu, F., Tian, L., Cai, Z., Wang, X., Liang, P., Wang, S., and Li, S.: What caused the lag between oxygen-18 and
647 deuterium excess in atmospheric vapor and precipitation during the earlier summer season in southwest China?,
648 J. Hydrol., 644, 10.1016/j.jhydrol.2024.132087, 2024.
649 Liu, J., Xiao, C., Ding, M., and Ren, J.: Variations in stable hydrogen and oxygen isotopes in atmospheric water
650 vapor in the marine boundary layer across a wide latitude range, Journal of Environmental Sciences, 26, 2266-
651 2276, 10.1016/j.jes.2014.09.007, 2014.
652 Luo, L.: Meteorological observation data from the integrated observation and research station of the alpine
653 environment in Southeast Tibet (2007-2017), National Tibetan Plateau Data Center [dataset],
654 10.11888/AtmosphericPhysics.tpe.68.db, 2018.
655 Ma, T., Jiang, Z., Ding, M., He, P., Li, Y., Zhang, W., and Geng, L.: A model framework for atmosphere–snow
656 water vapor exchange and the associated isotope effects at Dome Argus, Antarctica – Part 1: The diurnal changes,
657 The Cryosphere, 18, 4547-4565, 10.5194/tc-18-4547-2024, 2024.
658 Merlivat, L. and Jouzel, J.: Global climatic interpretation of the deuterium-oxygen 18 relationship for
659 precipitation, J. Geophys. Res., 84, 5029-5033, 1979.
660 Noone, D.: Pairing Measurements of the Water Vapor Isotope Ratio with Humidity to Deduce Atmospheric
661 Moistening and Dehydration in the Tropical Midtroposphere, J. Climate, 25, 4476-4494, 10.1175/jcli-d-11-
662 00582.1, 2012.
663 Pang, H., Hou, S., Kaspari, S., Mayewski, P., Introne, D., Masson-Delmotte, V., Jouzel, J., Li, Z., He, Y., Hong, S.,
664 and Qin, D.: Atmospheric circulation change in the central Himalayas indicated by a high-resolution ice core
665 deuterium excess record, Climate Research, 53, 1-12, 10.3354/cr01090, 2012.
666 Putman, A. L., Fiorella, R. P., Bowen, G. J., and Cai, Z.: A Global Perspective on Local Meteoric Water Lines:
667 Meta-analytic Insight into Fundamental Controls and Practical Constraints, Water Resour. Res., 55, 6896-6910,
668 10.1029/2019wr025181, 2019.
669 Risi, C., Bony, S., and Vimeux, F.: Influence of convective processes on the isotopic composition ($\delta^{18}O$ and δD)
670 of precipitation and water vapor in the tropics: 2. Physical interpretation of the amount effect, J. Geophys. Res.,
671 113, D19306, 10.1029/2008JD009943, 2008a.
672 Risi, C., Bony, S., Vimeux, F., Descroix, L., Ibrahim, B., Lebreton, E., Mamadou, I., and Sultan, B.: What controls
673 the isotopic composition of the African monsoon precipitation? Insights from event-based precipitation collected
674 during the 2006 AMMA field campaign, Geophys. Res. Lett., 35, L24808, 10.1029/2008GL035920, 2008b.
675 Ruan, J., Zhang, H., Cai, Z., Yang, X., and Yin, J.: Regional controls on daily to interannual variations of
676 precipitation isotope ratios in Southeast China: Implications for paleomonsoon reconstruction, Earth Planet. Sci.
677 Lett., 527, 115794, 10.1016/j.epsl.2019.115794, 2019.
678 Samuels-Crow, K. E., Galewsky, J., Sharp, Z. D., and Dennis, K. J.: Deuterium excess in subtropical free
679 troposphere water vapor: Continuous measurements from the Chajnantor Plateau, northern Chile, Geophys. Res.

Lett., 41, 8652-8659, 10.1002/2014gl062302, 2014.

Sayres, D. S., Pfister, L., Hanisco, T. F., Moyer, E. J., Smith, J. B., St. Clair, J. M., O'Brien, A. S., Witinski, M. F., Legg, M., and Anderson, J. G.: Influence of convection on the water isotopic composition of the tropical tropopause layer and tropical stratosphere, J. Geophys. Res., 115, 10.1029/2009JD013100, 2010.

Scholl, M. A., Shanley, J. B., Zegarra, J. P., and Coplen, T. B.: The stable isotope amount effect: New insights from NEXRAD echo tops, Luquillo Mountains, Puerto Rico, Water Resour. Res., 45, 10.1029/2008wr007515, 2009.

Shao, L., Tian, L., Cai, Z., Wang, C., and Li, Y.: Large-scale atmospheric circulation influences the ice core d-excess record from the central Tibetan Plateau, Clim. Dyn., 57, 1805-1816, 10.1007/s00382-021-05779-9, 2021.

Sodemann, H., Schwierz, C., and Wernli, H.: Interannual variability of Greenland winter precipitation sources: Lagrangian moisture diagnostic and North Atlantic Oscillation influence, J. Geophys. Res., 113, 10.1029/2007jd008503, 2008.

Sodemann, H., Aemisegger, F., Pfahl, S., Bitter, M., Corsmeier, U., Feuerle, T., Graf, P., Hankers, R., Hsiao, G., Schulz, H., Wieser, A., and Wernli, H.: The stable isotopic composition of water vapour above Corsica during the HyMeX SOP1 campaign: insight into vertical mixing processes from lower-tropospheric survey flights, Atmos. Chem. Phys., 17, 6125-6151, 10.5194/acp-17-6125-2017, 2017.

Steen-Larsen, H. C., Risi, C., Werner, M., Yoshimura, K., and Masson-Delmotte, V.: Evaluating the skills of isotope-enabled General Circulation Models against in-situ atmospheric water vapor isotope observations, J. Geophys. Res., 122, 246-263, 10.1002/2016JD025443, 2017.

Stein, A. F., Draxler, R. R., Rolph, G. D., Stunder, B. J. B., Cohen, M. D., and Ngan, F.: NOAA's HYSPLIT atmospheric transport and dispersion modeling system, Bull. Am. Meteorol. Soc., 96, 2059-2077, 10.1175/BAMS-D-14-00110.1, 2015.

Terzer-Wassmuth, S., Wassenaar, L. I., Welker, J. M., and Araguas-Araguas, L. J.: Improved High-Resolution Global and Regionalized Isoscapes of δ18O, δ2H, and d-Excess in Precipitation, Hydrol. Processes, 35, 10.1002/hyp.14254, 2021.

Thompson, L. G., Yao, T., E.Mosley-Thompson, Davis, M. E., Henderson, K. A., and Lin, P.-N.: A High-Resolution Millennial Record of the South Asian Monsoon from Himalayan Ice Cores, Science, 289, 1916-1919, 10.1126/science.289.5486.1916, 2000.

Thompson, L. G., Yao, T. D., Davis, M. E., Mosley-Thompson, E., Synal, H. A., Wu, G., Bolzan, J. F., Kutuzov, S., Beaudon, E., Sierra-Hernández, M. R., and Beer, J.: Ice core evidence for an orbital-scale climate transition on the Northwest Tibetan Plateau, Quat. Sci. Rev., 324, 10.1016/j.quascirev.2023.108443, 2024.

Tian, L., Masson-Delmotte, V., Stievenard, M., Yao, T., and Jouzel, J.: Tibetan Plateau summer monsoon northward extent revealed by measurements of water stable isotopes, J. Geophys. Res., 106, 28081-28088, 10.1029/2001JD900186, 2001.

Tian, L., Yao, T., MacClune, K., White, J. W. C., Schilla, A., Vaughn, B., Vachon, R., and Ichiyanagi, K.: Stable isotopic variations in west China: A consideration of moisture sources, J. Geophys. Res., 112, D10112, 10.1029/2006jd007718, 2007.

Tian, L., Yu, W., Schuster, P. F., Wen, R., Cai, Z., Wang, D., Shao, L., Cui, J., and Guo, X.: Control of seasonal water vapor isotope variations at Lhasa, southern Tibetan Plateau, J. Hydrol., 580, 124237, 10.1016/j.jhydrol.2019.124237, 2020.

Uemura, R., Matsui, Y., Yoshimura, K., Motoyama, H., and Yoshida, N.: Evidence of deuterium excess in water vapor as an indicator of ocean surface conditions, J. Geophys. Res., 113, 10.1029/2008jd010209, 2008.

Vuille, M., Bradley, R. S., Werner, M., Healy, R., and Keimig, F.: Modeling $\delta^{18}O$ in precipitation over the tropical Americas: 1. Interannual variability and climatic controls, J. Geophys. Res., 108, 4174, 10.1029/2001JD002038, 2003.

Wahl, S., Steen-Larsen, H. C., Hughes, A. G., Dietrich, L. J., Zuhr, A., Behrens, M., Faber, A.-K., and Hörhold,

M.: Atmosphere-Snow Exchange Explains Surface Snow Isotope Variability, Geophys. Res. Lett., 49, e2022GL099529, 10.1029/2022GL099529, 2022.

Webster, C. R. and Heymsfield, A. J.: Water isotope ratios D/H, 18O/16O, 17O/16O in and out of clouds map dehydration pathways, Science, 302, 1742-1745, 10.1126/science.1089496, 2003.

Wei, Z. and Lee, X.: The utility of near-surface water vapor deuterium excess as an indicator of atmospheric moisture source, J. Hydrol., 123923, 10.1016/j.jhydrol.2019.123923, 2019.

Welp, L. R., Lee, X., Griffis, T. J., Wen, X. F., Xiao, W., Li, S., Sun, X., Hu, Z., Val Martin, M., and Huang, J.: A meta-analysis of water vapor deuterium-excess in the midlatitude atmospheric surface layer, Global Biogeochem. Cycles, 26, 10.1029/2011gb004246, 2012.

Worden, J., Noone, D., and Bowman, K.: Importance of rain evaporation and continental convection in the tropical water cycle, Nature, 445, 528-532, 10.1038/nature05508, 2007.

Yang, X. and Yao, T.: Seasonality of moisture supplies to precipitation over the Third Pole: a stable water isotopic perspective, Sci Rep, 10, 15020, 10.1038/s41598-020-71949-0, 2020.

Yang, X., Davis, M. E., Acharya, S., and Yao, T.: Asian monsoon variations revealed from stable isotopes in precipitation, Clim. Dyn., 51, 2267-2283, 10.1007/s00382-017-4011-4, 2017.

Yao, T., Masson-Delmotte, V., Gao, J., Yu, W., Yang, X., Risi, C., Sturm, C., Werner, M., Zhao, H., He, Y., Ren, W., Tian, L., Shi, C., and Hou, S.: A review of climatic controls on $\delta^{18}O$ in precipitation over the Tibetan Plateau: Observations and simulations, Rev. Geophys., 51, 525-548, 10.1002/rog.20023, 2013.

Yao, T., Bolch, T., Chen, D., Gao, J., Immerzeel, W., Piao, S., Su, F., Thompson, L., Wada, Y., Wang, L., Wang, T., Wu, G., Xu, B., Yang, W., Zhang, G., and Zhao, P.: The imbalance of the Asian water tower, Nature Reviews Earth & Environment, 3, 618-632, 10.1038/s43017-022-00299-4, 2022.

Yu, W., Tian, L., Ma, Y., Xu, B., and Qu, D.: Simultaneous monitoring of stable oxygen isotope composition in water vapour and precipitation over the central Tibetan Plateau, Atmos. Chem. Phys., 15, 10251-10262, 10.5194/acp-15-10251-2015, 2015.

Yu, W., Tian, L., Risi, C., Yao, T., Ma, Y., Zhao, H., Zhu, H., He, Y., Xu, B., Zhang, H., and Qu, D.: $\delta^{18}O$ records in water vapor and an ice core from the eastern Pamir Plateau: Implications for paleoclimate reconstructions, Earth Planet. Sci. Lett., 456, 146-156, 10.1016/j.epsl.2016.10.001, 2016.

Zhang, Q., Shen, Z., Pokhrel, Y., Farinotti, D., Singh, V. P., Xu, C.-Y., Wu, W., and Wang, G.: Oceanic climate changes threaten the sustainability of Asia's water tower, Nature, 615, 87-93, 10.1038/s41586-022-05643-8, 2023.

Zhang, Q., Shen, Z., Pokhrel, Y., Farinotti, D., Singh, V. P., Xu, C.-Y., Wu, W., and Wang, G.: Reply to: Atlantic oceanic droughts do not threaten Asian water tower, Nature, 638, E16-E18, 10.1038/s41586-024-08358-0, 2025.

Zhao, H., Xu, B., Li, Z., Wang, M., Li, J., and Zhang, X.: Abundant climatic information in water stable isotope record from a maritime glacier on southeastern Tibetan Plateau, Clim. Dyn., 48, 1161-1171, 10.1007/s00382-016-3133-4, 2017.

Zhao, H., Xu, B., Yao, T., Wu, G., Lin, S., Gao, J., and Wang, M.: Deuterium excess record in a southern Tibetan ice core and its potential climatic implications, Clim. Dyn., 38, 1791-1803, 10.1007/s00382-011-1161-7, 2012.

Zhao, Y., Xu, C., Yu, X., Liu, Y., and Ji, X.: Atlantic oceanic droughts do not threaten Asian water tower, Nature, 638, E13-E15, 10.1038/s41586-024-08357-1, 2025.